

Cite this: *J. Mater. Chem. A*, 2021, 9, 19631Received 25th March 2021  
Accepted 6th May 2021

DOI: 10.1039/d1ta02504j

rsc.li/materials-a

Achieving selective photocatalytic CO<sub>2</sub> reduction to CO on bismuth tantalum oxyhalogen nanoplates†Xiaoping Tao,<sup>‡a</sup> Yi Wang,<sup>‡ab</sup> Jiangshan Qu,<sup>ab</sup> Yue Zhao,<sup>a</sup> Rengui Li<sup>ID</sup><sup>\*a</sup> and Can Li<sup>ID</sup><sup>\*a</sup>

The photocatalytic conversion of carbon dioxide to fuels presents great promise for storing renewable energy and alleviating global warming. Herein, using the visible-light-responsive semiconductor bismuth tantalum oxyhalogen (Bi<sub>4</sub>TaO<sub>8</sub>X, X = Cl, Br) with suitable band structures, we realize the photocatalytic reduction of CO<sub>2</sub> to selectively produce CO under visible light without introducing any sacrificial reagents. An isotope-labeling experiment clearly demonstrated that the produced CO originated from CO<sub>2</sub> and, additionally, continuous water oxidation for O<sub>2</sub> evolution was also detected during photocatalytic CO<sub>2</sub> reduction. Further introducing crystal morphology modulation to prepare well-defined nanocrystals enables great enhancement of the photogenerated charge separation performance compared to that of irregular nanoparticles. Moreover, surface modification of the silver nanoparticles deployed as the CO<sub>2</sub> reduction cocatalyst evidently facilitates the generation of intermediate species to promote the surface catalytic reaction. This work not only presents a potential semiconductor candidate for photocatalytic CO<sub>2</sub> reduction, but it also provides a feasible strategy for designing artificial photosynthetic systems *via* combining morphology tailoring and suitable cocatalysts.

Artificial photosynthesis mimicking the process in green plants to realize the conversion and storage of solar energy and atmospheric CO<sub>2</sub> gas into high-value-added carbon-containing compounds is of profound fundamental importance for coping with global warming and energy problems.<sup>1–3</sup> However, the photocatalytic conversion of abundant CO<sub>2</sub> using H<sub>2</sub>O as a proton source offers both promise and challenges, especially given the relatively inert nature of CO<sub>2</sub> molecules and the multi-electron reaction process.<sup>4,5</sup> Although the use of semiconductor-

based photocatalysts for photocatalytic CO<sub>2</sub> reduction has received increasing attention since the first pioneering work in 1978,<sup>6</sup> the progress has been limited by poor charge separation and sluggish reaction kinetics. To achieve the CO<sub>2</sub> reduction reaction using H<sub>2</sub>O as the proton source, the photogenerated charges in semiconductors must separate, transfer to the surface, and then react with the absorbed molecules, giving rise to the photoassisted splitting of H<sub>2</sub>O to release oxygen and produce carbon-containing compounds. Additionally, the thermodynamic requirements necessitate semiconductor photocatalysts with suitable band positions to ensure that the photoexcited electrons and holes are endowed with sufficient energy to reduce CO<sub>2</sub> and oxidize H<sub>2</sub>O simultaneously.<sup>7</sup>

The challenges in photocatalytic CO<sub>2</sub> conversion include not only the difficult activation of CO<sub>2</sub> and the sophisticated reaction kinetics, but also the notoriously fast recombination and deficient separation of the photogenerated charge carriers of the photocatalysts.<sup>2</sup> Endeavors in the past few decades have resulted in the development of strategies including surface decoration of suitable cocatalysts, size control, and surface defect engineering of stoichiometric photocatalysts to promote the efficiency and selectivity of photocatalytic CO<sub>2</sub> reduction.<sup>8–10</sup> For instance, the decoration of an atomic-cobalt-based cocatalyst on W<sub>18</sub>O<sub>49</sub> nanowires enabled the acceleration of the electron transport and modified the energy configuration, resulting in impressive CO generation.<sup>11</sup> It was reported that the assembly of a BiOBr photocatalyst with abundant oxygen vacancies could tailor the electronic band structure and capture photoinduced carriers to benefit the separation and stabilize the intermediates to reduce the activation energy barrier.<sup>12</sup> Although progress has been made, the overwhelming majority of published reports so far have concentrated on CO<sub>2</sub> reduction in the presence of various easily oxidized reagents including alcohols or amines to donate electrons, producing carbon-containing products at the cost of these sacrificial reagents. Even in the overall reduction of CO<sub>2</sub> using H<sub>2</sub>O as the sole proton source, the detection of water oxidation is scarcely considered, despite the nonnegligible significance of water oxidation in photosynthesis.<sup>13</sup> The water

<sup>a</sup>State Key Laboratory of Catalysis, Dalian Institute of Chemical Physics, Chinese Academy of Sciences, Dalian National Laboratory for Clean Energy, Zhongshan Road 457, Dalian, 116023, China. E-mail: rgli@dicp.ac.cn; canli@dicp.ac.cn

<sup>b</sup>University of Chinese Academy of Sciences, China

† Electronic supplementary information (ESI) available. See DOI: 10.1039/d1ta02504j

‡ These two authors contributed equally to the work.

oxidation reaction to evolve oxygen or hydroxyl radicals in parallel with the CO<sub>2</sub> reduction reaction is recognized as the bottleneck, with a sluggish kinetics and complex proton-coupled electron transfer process.<sup>14</sup> Moreover, the detection of oxygen is even harder given the fact that the evolved oxygen and hydroxyl radicals tend to be adsorbed on the surface of photocatalysts and to oxidize the CO<sub>2</sub>-reduced intermediates and interrupt the reduction; consequently, few reported works have referred to the oxidation reaction so far. Reliable detection of water oxidation was reported on a SiC@MoS<sub>2</sub> Z-scheme photocatalyst that could achieve the overall conversion of CO<sub>2</sub> with H<sub>2</sub>O and yielded CH<sub>4</sub> and a stoichiometric ratio of O<sub>2</sub> at the same time.<sup>15</sup> A fundamental reason for the challenging nature of the water oxidation reaction in the overall photocatalytic reduction of CO<sub>2</sub> is the relatively inferior photocatalytic water oxidation ability of many semiconductors in terms of thermodynamics and kinetics.

Bismuth tantalum oxygen halogen (Bi<sub>4</sub>TaO<sub>8</sub>X, X = Cl, Br) is a class of typical Sillén–Aurivillius compounds with layered perovskite structures that have excellent light harvesting properties.<sup>16</sup> We previously reported the fabrication of a series of Bi<sub>4</sub>TaO<sub>8</sub>X photocatalysts that are able to achieve photocatalytic hydrogen reduction and the oxygen evolution reaction, especially their decent performance in photocatalytic water oxidation under the irradiation of visible light.<sup>17,18</sup> Furthermore, the intrinsic layered structure makes it feasible to achieve morphology tuning as well as efficient photogenerated charge separation. Although Bi<sub>4</sub>TaO<sub>8</sub>X photocatalysts possess unique crystalline structures and water oxidation capabilities, little research has focused on this series of materials to date, except one previous study on the conversion of CO<sub>2</sub> to CH<sub>4</sub> over this semiconductor, which did not mention the detection of water oxidation during the process.<sup>19</sup> This shows the need for further insight into the exploration of photocatalytic CO<sub>2</sub> reduction on these promising materials.

Herein, we report that the selective photocatalytic conversion of CO<sub>2</sub> to CO can be realized on visible-light-responsive bismuth tantalum oxygen halogen under visible light irradiation, and that the oxidation of water to O<sub>2</sub> can also be detected simultaneously. Two determining factors, morphology regulation, which significantly tunes the photogenerated charge separation process, and surface decoration of a silver cocatalyst, which promotes the absorption and generation of intermediates, together result in a great enhancement in photocatalytic CO<sub>2</sub> reduction, thereby providing a feasible strategy to assemble efficient photocatalysts for the photoassisted reduction of CO<sub>2</sub> into valuable chemicals.

The crystalline structure of bismuth tantalum oxygen halogen (Bi<sub>4</sub>TaO<sub>8</sub>X, X = Cl, Br) is shown in Fig. 1a. It is composed of slices of [Bi<sub>2</sub>O<sub>2</sub>] and layers of [TaO<sub>6</sub>] octahedra, intercalated with halogen atoms. The intrinsic layered structure is expected to form two-dimensional morphologies, which exhibit superiority in photogenerated charge separation and transfer in photocatalysis.<sup>20,21</sup> The Bi<sub>4</sub>TaO<sub>8</sub>X was verified to have a band gap of approximately 2.6 eV with the conduction band and valence band located at approximately −0.9 and 1.7 eV vs. NHE (pH = 7), respectively, which could meet the

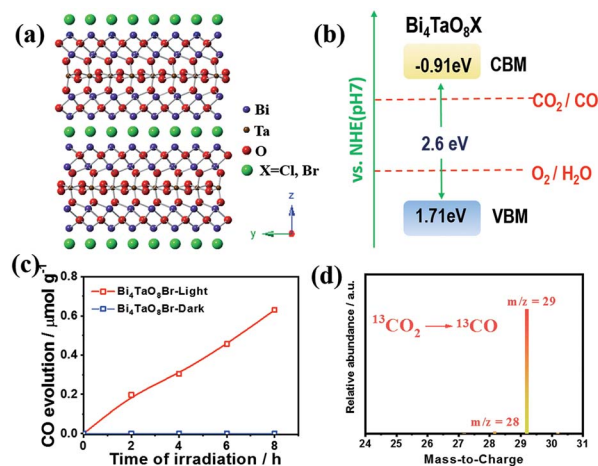


Fig. 1 (a) The crystal structure of Bi<sub>4</sub>TaO<sub>8</sub>X (X = Cl, Br). (b) A schematic illustration of the band structure of Bi<sub>4</sub>TaO<sub>8</sub>X (X = Cl, Br). (c) The time course of photocatalytic CO<sub>2</sub> reduction on Bi<sub>4</sub>TaO<sub>8</sub>Br. (d) GC-MS analysis of the generated CO using <sup>13</sup>CO<sub>2</sub> as the feedstock.

thermodynamic requirements for water oxidation and the reduction of CO<sub>2</sub> to multiple products including CO (Fig. 1b). Notably, Bi<sub>4</sub>TaO<sub>8</sub>X demonstrated good photocatalytic water oxidation capability under visible light irradiation, making it a candidate for the photocatalytic overall CO<sub>2</sub> conversion reaction.

Bi<sub>4</sub>TaO<sub>8</sub>X (X = Cl, Br) was synthesized *via* a traditional solid-state reaction, in which stoichiometric amounts of the precursors Bi<sub>2</sub>O<sub>3</sub>, Ta<sub>2</sub>O<sub>5</sub>, and BiOX were mixed and sealed in a vacuum quartz tube, followed by calcination at 973 K for 14 hours. Using the as-prepared Bi<sub>4</sub>TaO<sub>8</sub>Br as the photocatalyst, we found that surprisingly, photocatalytic CO<sub>2</sub> reduction could be realized in the presence of H<sub>2</sub>O without introducing any sacrificial reagents, and CO was observed as the sole product with a selectivity of 100% and no other products being detected (Fig. 1c). To directly track the origin of the produced CO, an isotope labelling experiment using <sup>13</sup>CO<sub>2</sub> as the input was performed. As shown in Fig. 1d, the result of gas chromatography-mass spectrometry (GC-MS) analysis showed the production of <sup>13</sup>CO, clearly evidencing that CO originated from the input CO<sub>2</sub>, although the photocatalytic activity was not high. Considering that the activity may be limited by the poor charge separation and transfer for Bi<sub>4</sub>TaO<sub>8</sub>Br, flux treatment was utilized in the preparation process, and the corresponding sample was labelled as Bi<sub>4</sub>TaO<sub>8</sub>Br-F. As shown in Fig. 2a and b, unlike the irregular Bi<sub>4</sub>TaO<sub>8</sub>Br nanoparticles, Bi<sub>4</sub>TaO<sub>8</sub>Br-F exhibits a nanoplate morphology with a diameter of ~500 nm (Fig. S1†). XRD patterns of the two samples were consistent with the standard card for the pure phase and showed negligible differences between each other (Fig. S2†). Raman spectra were also collected, and no obvious variation was observed between the spectrum of the Bi<sub>4</sub>TaO<sub>8</sub>Br nanoparticles and that of the nanoplates, indicating no changes in the phase or bonding situation during the process of flux treatment (Fig. S3†). UV-visible spectra also depicted a comparable result in the light absorption range (Fig. S4†). However, as shown in Fig. 2c, when

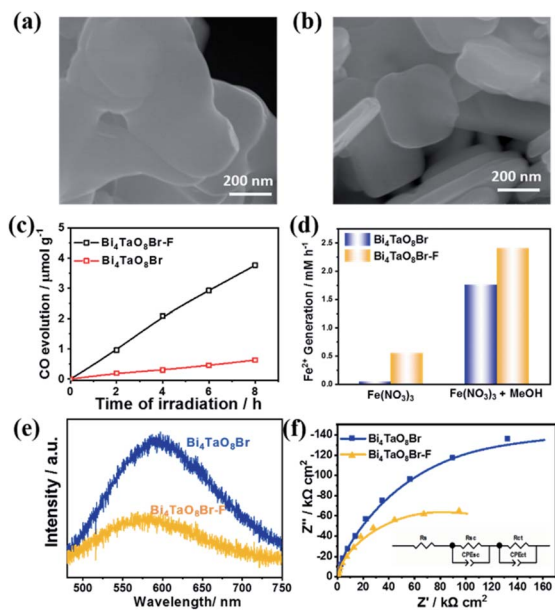


Fig. 2 (a and b) SEM images of  $\text{Bi}_4\text{TaO}_8\text{Br}$  and  $\text{Bi}_4\text{TaO}_8\text{Br-F}$ . (c) The time course of photocatalytic  $\text{CO}_2$  reduction on  $\text{Bi}_4\text{TaO}_8\text{Br}$  and  $\text{Bi}_4\text{TaO}_8\text{Br-F}$ . (d) Photocatalytic reactions on  $\text{Bi}_4\text{TaO}_8\text{Br}$  and  $\text{Bi}_4\text{TaO}_8\text{Br-F}$  in the presence of  $\text{Fe}(\text{NO}_3)_3$  and  $\text{CH}_3\text{OH}$ . (e) Steady photoluminescence (PL) spectra of  $\text{Bi}_4\text{TaO}_8\text{Br}$  and  $\text{Bi}_4\text{TaO}_8\text{Br-F}$  at room temperature. (f) Electrochemical impedance spectra (EIS) of  $\text{Bi}_4\text{TaO}_8\text{Br}$  and  $\text{Bi}_4\text{TaO}_8\text{Br-F}$  and the corresponding equivalent circuit.

the photocatalytic  $\text{CO}_2$  reduction was conducted under light irradiation, the photocatalytic activity of the flux-treated  $\text{Bi}_4\text{TaO}_8\text{Br}$  nanoplates obviously showed enhanced photocatalytic reduction of  $\text{CO}_2$  to  $\text{CO}$  compared to the  $\text{Bi}_4\text{TaO}_8\text{Br}$  nanoparticles.

To determine the influence of flux treatment on the photo-generated charge separation, both electron-consuming and hole-consuming reagents were introduced. It was assumed that both charge-consuming reactions were kinetically fast enough. We chose the photocatalytic conversion of  $\text{Fe}^{3+}$  to  $\text{Fe}^{2+}$  to probe the electrons and the oxidation of  $\text{CH}_3\text{OH}$  molecules for capturing holes; the conversion of  $\text{Fe}^{3+}$  to  $\text{Fe}^{2+}$  can be used as an index for activity evaluation. As demonstrated in Fig. 2d,  $\text{Bi}_4\text{TaO}_8\text{Br-F}$  exhibited superior  $\text{Fe}^{3+}$  conversion performance in the presence of  $\text{CH}_3\text{OH}$  as a result of the high activity of the oxidation half-reaction. The enhancement compared to  $\text{Bi}_4\text{TaO}_8\text{Br}$  implies that the charge separation efficiency of  $\text{Bi}_4\text{TaO}_8\text{Br-F}$  is higher than that of  $\text{Bi}_4\text{TaO}_8\text{Br}$  synthesized without flux treatment. Additionally, the water oxidation on the surface of  $\text{Bi}_4\text{TaO}_8\text{Br-F}$  is superior to that of  $\text{Bi}_4\text{TaO}_8\text{Br}$  in view of its higher conversion activity without  $\text{CH}_3\text{OH}$ . Correspondingly, the steady photoluminescence (PL) spectrum of  $\text{Bi}_4\text{TaO}_8\text{Br-F}$  exhibits a significantly decreased intensity of radiative recombination compared to that of  $\text{Bi}_4\text{TaO}_8\text{Br}$ , implying more inhibited recombination over the same period (Fig. 2e). In addition, electrochemical impedance spectra (EIS) were also carried out to evaluate the charge separation properties for  $\text{Bi}_4\text{TaO}_8\text{Br}$  and  $\text{Bi}_4\text{TaO}_8\text{Br-F}$ . As can be seen in Fig. 2f, the fitting results showed smaller resistance values for  $\text{Bi}_4\text{TaO}_8\text{Br-F}$  in

both the space charge region and the process of charge transfer from the semiconductor to the surface reactants compared to those of  $\text{Bi}_4\text{TaO}_8\text{Br}$  (Fig. S5<sup>†</sup>), indicating better charge separation and transfer properties in  $\text{Bi}_4\text{TaO}_8\text{Br-F}$ . Moreover, the charge separation efficiency calculated from the  $J-V$  curves in the presence of the hole acceptor further demonstrated the enhanced photogenerated charge separation in  $\text{Bi}_4\text{TaO}_8\text{Br-F}$ , which parallels the EIS and PL results (Fig. S6<sup>†</sup>). Similar results were also obtained for  $\text{Bi}_4\text{TaO}_8\text{Cl}$  and  $\text{Bi}_4\text{TaO}_8\text{Cl-F}$  (Fig. S7–S9<sup>†</sup>). The above results demonstrate that flux treatment greatly improves the photogenerated charge separation properties of  $\text{Bi}_4\text{TaO}_8\text{X}$  ( $\text{X} = \text{Cl}, \text{Br}$ ).

As mentioned above, even if the photogenerated charge separation is satisfactory, the photocatalytic  $\text{CO}_2$  reaction is limited by the poor surface catalytic reaction. To promote the photocatalytic conversion of  $\text{CO}_2$  to  $\text{CO}$ , different kinds of surface cocatalysts (namely, Au, Ag, Pd, Ir, Rh and Cu) were loaded on the surface of  $\text{Bi}_4\text{TaO}_8\text{Br-F}$ , given its robust performance in electrocatalytic  $\text{CO}_2$  reduction.<sup>22,23</sup> As shown in Fig. 3a, decoration with Au, Ag and Pd resulted in enhanced CO evolution compared to that of bare  $\text{Bi}_4\text{TaO}_8\text{Br-F}$ , while the others cocatalysts resulted in negative effects, which might be attributed to the mismatch between the semiconductor and the cocatalysts. Surprisingly, Ag was found to be the best cocatalyst for photocatalytic  $\text{CO}_2$  reduction on  $\text{Bi}_4\text{TaO}_8\text{Br-F}$ , and further optimization of the loading amount demonstrated a plateau in the CO evolution at a weight of 1%. Various oxide-based cocatalysts, namely,  $\text{MnO}_x$ ,  $\text{CoO}_x$ ,  $\text{ZnO}_2$ ,  $\text{ZrO}_2$ , and  $\text{MgO}$  were also preliminarily introduced; unfortunately, none of these could work yet (Fig. S10 & S11<sup>†</sup>). Photocatalytic stability testing of Ag- $\text{Bi}_4\text{TaO}_8\text{Br-F}$  was also carried out for more than three cycles with each reaction cycle being 4 hours (Fig. 3c). The result suggests that Ag- $\text{Bi}_4\text{TaO}_8\text{Br-F}$  is able to realize the stable conversion of  $\text{CO}_2$  to  $\text{CO}$ , and only a slight decrease was observed after three cycling tests. Furthermore, the water oxidation product was also tracked during the photocatalytic  $\text{CO}_2$  reduction *via* a linkage with an online gas detection system. As expected, the appearance of an obvious  $\text{O}_2$  peak was observed *via* GC, and the intensity of the signal gradually increased with the reaction time, as shown in Fig. 3d. Although the amount of  $\text{O}_2$  is still very low and the production of  $\text{CO}$  could not be analysed simultaneously, the significant  $\text{O}_2$  peak strongly verified that the water oxidation half-reaction proceeded, which means the overall photocatalytic  $\text{CO}_2$  reduction with  $\text{H}_2\text{O}$  could indeed take place on the semiconductor Ag- $\text{Bi}_4\text{TaO}_8\text{Br-F}$ . Notably, given the low solubility of  $\text{CO}_2$  in water, all the photocatalytic experiments were conducted in a saturated  $\text{KHCO}_3$  solution; the photocatalytic performance in pure water was also demonstrated in Fig. S12.<sup>†</sup>

The roles of the Ag cocatalyst in the photocatalytic reaction were then investigated to better understand the reaction mechanism. As can be seen in Fig. 4a, Ag nanoparticles with diameters of  $\sim 5\text{--}20$  nm were dispersed on the surface of the  $\text{Bi}_4\text{TaO}_8\text{Br-F}$  nanoplates (Fig. S13 & S14<sup>†</sup>). High-resolution transmission electron microscopy (HRTEM) provided great insight into the surface microstructure of Ag-loaded  $\text{Bi}_4\text{TaO}_8\text{Br-F}$ , as shown in Fig. 4b. The clear lattice fringes indicate the good



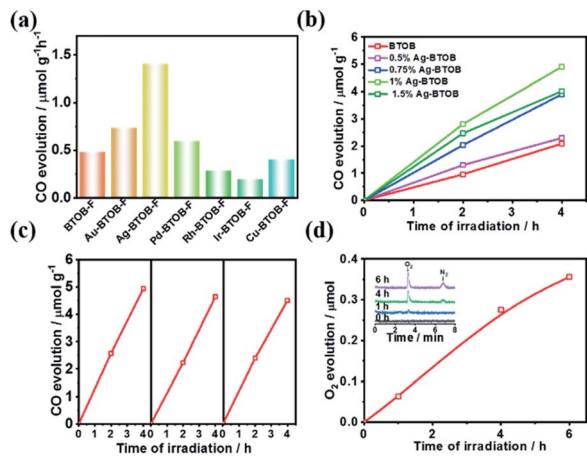


**Fig. 3** (a) The photocatalytic activity of CO<sub>2</sub> reduction on Bi<sub>4</sub>TaO<sub>8</sub>Br-F loaded with different cocatalysts. (b) The time courses of photocatalytic CO<sub>2</sub> reduction on Bi<sub>4</sub>TaO<sub>8</sub>Br-F loaded with different amounts of Ag. (c) Cycling tests of photocatalytic CO<sub>2</sub> reduction on Ag-Bi<sub>4</sub>TaO<sub>8</sub>Br-F. (d) The time course of oxygen evolution during photocatalytic CO<sub>2</sub> reduction on Ag-Bi<sub>4</sub>TaO<sub>8</sub>Br-F under UV light irradiation; inset: GC signals of O<sub>2</sub> and N<sub>2</sub> after different reaction times.

crystallinity of both the cocatalyst and the semiconductor, where the lattice spacing of 0.233 nm is consistent with the (111) lattice plane of metallic Ag, while the observed lattice distance of 0.381 nm corresponds well with the (110) facet of Bi<sub>4</sub>TaO<sub>8</sub>Br. The Ag nanoparticles were in intimate contact with the semiconductor, which is conducive to better synergy. In addition, the chemical states of the Ag cocatalyst as well as the interaction between Ag and Bi<sub>4</sub>TaO<sub>8</sub>Br-F were investigated using XPS (X-ray photoelectron spectroscopy) (Fig. 4c). The XPS spectra of Bi, Ta and O showed slight shifts to higher bonding energy, which could be due to electron transfer from Bi<sub>4</sub>TaO<sub>8</sub>Br to Ag, implying intimate contact between Bi<sub>4</sub>TaO<sub>8</sub>Br and Ag (Fig. S15<sup>†</sup>).<sup>24</sup> In addition, the fine spectrum of Ag showed the coexistence of peaks at 373.8 and 367.8 eV, which is due to spin-orbit splitting according to the literature, indicating the presence of the metallic state of Ag<sup>0</sup>, which agrees well with the HRTEM analysis.<sup>25,26</sup> The Ag nanoparticles on the surface show some aggregation after the cycling reaction, and the structural characterizations of Ag-Bi<sub>4</sub>TaO<sub>8</sub>Br-F after the photocatalytic reactions indicate that it maintained similar phase and chemical states on the surface to the fresh material (Fig. S16–S18<sup>†</sup>). Furthermore, the influence of Ag on the CO<sub>2</sub> absorption was also investigated, as shown in Fig. 4d, in which surface loading of the Ag cocatalyst resulted in obviously enhanced absorption of CO<sub>2</sub> molecules compared to pristine Bi<sub>4</sub>TaO<sub>8</sub>Br, implying that the Ag on the surface could facilitate the process of CO<sub>2</sub> absorption.

To explore the possible mechanism of CO<sub>2</sub> conversion on Bi<sub>4</sub>TaO<sub>8</sub>Br, *in situ* Fourier Transform Infrared Spectrum (FTIR) was utilized to provide decisive evidence regarding the intermediate products and reaction pathways. Significant CO<sub>2</sub> adsorption could be observed from the vibrational mode of (C=O) at 2295 and 2380 cm<sup>-1</sup> (Fig. S19<sup>†</sup>). As shown in Fig. 4e and f, various carbon-containing reaction intermediates, including

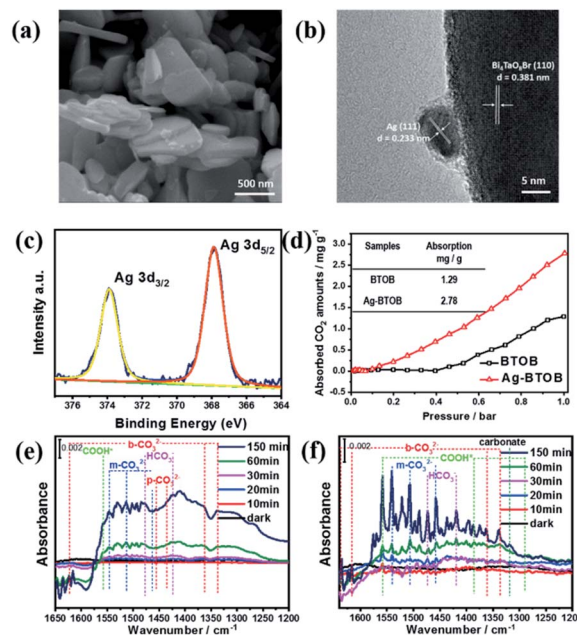
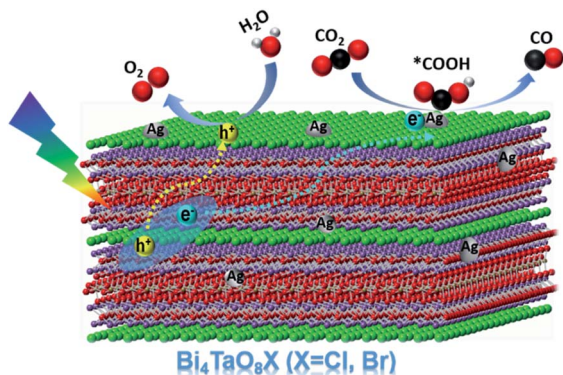


**Fig. 4** (a and b) SEM and HRTEM image of Bi<sub>4</sub>TaO<sub>8</sub>Br-F loaded with Ag. (c) The XPS fine spectrum of silver in Ag-Bi<sub>4</sub>TaO<sub>8</sub>Br-F. (d) The absorption curves of CO<sub>2</sub> on Bi<sub>4</sub>TaO<sub>8</sub>Br-F and Ag-Bi<sub>4</sub>TaO<sub>8</sub>Br-F at room temperature. (e and f) *In situ* FTIR spectra of photocatalytic CO<sub>2</sub> reduction on Bi<sub>4</sub>TaO<sub>8</sub>Br-F and Ag-Bi<sub>4</sub>TaO<sub>8</sub>Br-F.

bicarbonate (HCO<sub>3</sub><sup>-</sup>, 1473 and 1419 cm<sup>-1</sup>), bidentate carbonate (b-CO<sub>3</sub><sup>2-</sup>, 1338, 1363, 1616, and 1635 cm<sup>-1</sup>), and monodentate carbonate (m-CO<sub>3</sub><sup>2-</sup>, 1558, 1541, 1508 and 1457 cm<sup>-1</sup>) corresponding to adsorbed CO<sub>2</sub> species were detected during the photocatalytic reaction, and all of these species gradually increased as the reaction proceeded. Compared to bare Bi<sub>4</sub>TaO<sub>8</sub>Br-F, the Ag-loaded Bi<sub>4</sub>TaO<sub>8</sub>Br-F demonstrated signals with stronger intensities within the same period, which could be attributed to the more intensive of CO<sub>2</sub> absorption ability and activation on Ag-Bi<sub>4</sub>TaO<sub>8</sub>Br-F. Additionally, the peaks located at 1588, 1386 and 1288 cm<sup>-1</sup> were assigned to the symmetric and antisymmetric OCO vibrations and C=O stretching of \*COOH, respectively,<sup>27,28</sup> which is consistent with previous experimental and theoretical studies claiming that the conversion of CO<sub>2</sub> to CO usually proceeds *via* a \*COOH intermediate coordinated to the catalyst surface.<sup>29,30</sup> As depicted in Fig. 4e and f, the Ag-loaded Bi<sub>4</sub>TaO<sub>8</sub>Br-F showed more significant surface intermediate signals compared to bare Bi<sub>4</sub>TaO<sub>8</sub>Br-F, which further certifies that the surface assembled with the Ag cocatalyst is favourable for CO<sub>2</sub> activation (\*COOH formation), thus promoting the overall conversion of CO<sub>2</sub> to CO.

Based on the above results, a plausible mechanism for the photocatalytic conversion of CO<sub>2</sub> to CO on Ag-Bi<sub>4</sub>TaO<sub>8</sub>Br-F was proposed (Scheme 1). Bi<sub>4</sub>TaO<sub>8</sub>Br was irradiated under visible light to generate electrons and holes with high energy, which could effectively separate and transfer to the surface due to the layer-structured properties with superior charge separation capability. The reduction of CO<sub>2</sub> to CO on the surface usually consists of two elementary steps, the first of which is the reductive adsorption of CO<sub>2</sub> on the catalyst surface involving



Scheme 1 The proposed mechanism of photocatalytic CO<sub>2</sub> reduction to CO on Bi<sub>4</sub>TaO<sub>8</sub>X.

a proton-coupled electron transfer process to form a \*COOH intermediate, where \* indicates the corresponding adsorption states of surface species. The adsorbed \*COOH intermediate is further reduced to \*CO *via* a concerted electron–proton transfer, and then desorbed from the catalyst surface. Ag has been shown to be an ideal electrocatalyst endowed with an appropriate adsorption strength for the key intermediate \*COOH,<sup>31–33</sup> and the cocatalyst on the surface with a relatively low Fermi level has also been proven to be capable of electron trapping and to further enhance the photogenerated charge separation,<sup>34</sup> which is assumed to promote the reduction of CO<sub>2</sub> to CO. Given the capability of Bi<sub>4</sub>TaO<sub>8</sub>Br for photocatalytic water oxidation, the water oxidation half-reaction to consume photogenerated holes is expected to take place on the surface of Bi<sub>4</sub>TaO<sub>8</sub>Br. Ultimately, the loading of the Ag cocatalyst promotes the CO<sub>2</sub> reduction reaction on the surface, combined with morphology tuning, which promotes the process of photogenerated charge separation and transport, contributes to the realization of overall photocatalytic CO<sub>2</sub> conversion on the Bi<sub>4</sub>TaO<sub>8</sub>Br photocatalyst.

## Conclusions

In conclusion, we have presented the achievement of the photocatalytic reduction of CO<sub>2</sub> to CO on the semiconductor Bi<sub>4</sub>TaO<sub>8</sub>X (X = Cl, Br) using H<sub>2</sub>O as the electron donor under visible light irradiation. During the photocatalytic reduction of CO<sub>2</sub> by the photogenerated electrons, the oxidation of H<sub>2</sub>O to O<sub>2</sub> by photogenerated holes takes place simultaneously. Through the morphology modulation, the flux-treated nanoplates demonstrate greatly enhanced charge separation and transfer properties compared to irregular nanoparticles. Further decoration with the cocatalyst Ag was proven to be favourable for the adsorption and activation of CO<sub>2</sub> and the generation of key intermediates, further promoting the overall CO<sub>2</sub> reduction reaction. This work not only presents a potential semiconductor candidate for photocatalytic CO<sub>2</sub> reduction, but also provides a feasible strategy combining morphology tailoring and appropriate cocatalysts in the hope of designing and recreating efficiently implemented artificial photosynthetic systems.

## Conflicts of interest

There are no conflicts to declare.

## Acknowledgements

This work was financially supported by the National Natural Science Foundation of China (22088102, 22090033) and Key Research Program of Frontier Sciences of Chinese Academy of Sciences (QYZDY-SSW-JSC023).

## References

- X. Liu, J. Iocozzia, Y. Wang, X. Cui, Y. Chen, S. Zhao, Z. Li and Z. Lin, *Energy Environ. Sci.*, 2017, **10**, 402–434.
- J. Fu, K. Jiang, X. Qiu, J. Yu and M. Liu, *Mater. Today*, 2020, **32**, 222–243.
- D. Li, B. Cen, C. Fang, X. Leng, W. Wang, Y. Wang, J. Chen and M. Luo, *New J. Chem.*, 2021, **45**, 561–568.
- G. Zhao, X. Huang, X. Wang and X. Wang, *J. Mater. Chem. A*, 2017, **5**, 21625–21649.
- X. Li, S. Wang, L. Li, X. Zu, Y. Sun and Y. Xie, *Accounts Chem. Res.*, 2020, **53**, 2964–2974.
- M. Halmann, *Nature*, 1978, **275**, 115–116.
- H. Shen, T. Peppel, J. Strunk and Z. Sun, *Solar RRL*, 2020, **4**, 1900546.
- X. Li, J. Yu, M. Jaroniec and X. Chen, *Chem. Rev.*, 2019, **119**, 3962–4179.
- D. Chen, X. Zhang and A. F. Lee, *J. Mater. Chem. A*, 2015, **3**, 14487–14516.
- W. Tu, Y. Zhou and Z. Zou, *Adv. Mater.*, 2014, **26**, 4607–4626.
- H. Zhang, Y. Wang, S. Zuo, W. Zhou, J. Zhang and X. W. D. Lou, *J. Am. Chem. Soc.*, 2021, **143**, 2173–2177.
- J. Di, C. Zhu, M. Ji, M. Duan, R. Long, C. Yan, K. Gu, J. Xiong, Y. She, J. Xia, H. Li and Z. Liu, *Angew. Chem., Int. Ed.*, 2018, **57**, 14847–14851.
- Y. Wang and T. He, *J. Mater. Chem. A*, 2021, **9**, 87–110.
- N.-T. Suen, S.-F. Hung, Q. Quan, N. Zhang, Y.-J. Xu and H. M. Chen, *Chem. Soc. Rev.*, 2017, **46**, 337.
- Y. Wang, X. Shang, J. Shen, Z. Zhang, D. Wang, J. Lin, J. C. S. Wu, X. Fu, X. Wang and C. Li, *Nat. Commun.*, 2020, **11**, 3043.
- A. M. Kusainova, W. Zhou, J. T. S. Irvine and P. Lightfoot, *J. Solid State Chem.*, 2002, **166**, 148–157.
- X. Tao, Y. Zhao, L. Mu, S. Wang, R. Li and C. Li, *Adv. Energy Mater.*, 2018, **8**, 1701392.
- X. Tao, Y. Gao, S. Wang, X. Wang, Y. Liu, Y. Zhao, F. Fan, M. Dupuis, R. Li and C. Li, *Adv. Energy Mater.*, 2019, **9**, 1803951.
- L. Li, Q. Han, L. Tang, Y. Zhang, P. Li, Y. Zhou and Z. Zou, *Nanoscale*, 2018, **10**, 1905–1911.
- Q. Lu, Y. Yu, Q. Ma, B. Chen and H. Zhang, *Adv. Mater.*, 2016, **28**, 1917.
- D. Qin, Y. Zhou, W. Wang, C. Zhang, G. Zeng, D. Huang, L. Wang, H. Wang, Y. Yang, L. Lei, S. Chen and D. He, *J. Mater. Chem. A*, 2020, **8**, 19156–19195.

- 22 G. Wang, J. Chen, Y. Ding, P. Cai, L. Yi, Y. Li, C. Tu, Y. Hou, Z. Wen and L. Dai, *Chem. Soc. Rev.*, 2021, **50**, 4993–5061.
- 23 J. Li and J. Gong, *Energy Environ. Sci.*, 2020, **13**, 3748–3779.
- 24 B. Zeng, S. Wang, Y. Gao, G. Li, W. Tian, J. Meeprasert, H. Li, H. Xie, F. Fan, R. Li and C. Li, *Adv. Funct. Mater.*, 2021, **31**, 2005688.
- 25 T. Takayama, H. Nakanishi, M. Matsui, A. Iwase and A. Kudo, *J. Photochem. Photobiol., A*, 2018, **358**, 416–421.
- 26 G. B. Hoflund, J. F. Weaver and W. S. Epling, *Surf. Sci. Spectra*, 1994, **3**, 151–156.
- 27 S. Kattel, W. Yu, X. Yang, B. Yan, Y. Huang, W. Wan, P. Liu and J. G. Chen, *Angew. Chem., Int. Ed.*, 2016, **55**, 7968–7973.
- 28 L. C. Grabow and M. Mavrikakis, *ACS Catal.*, 2011, **1**, 365–384.
- 29 H. Xie, S. Chen, F. Ma, J. Liang, Z. Miao, T. Wang, H. L. Wang, Y. Huang and Q. Li, *ACS Appl. Mater. Interfaces*, 2018, **10**, 36996–37004.
- 30 X. Jiao, X. Li, X. Jin, Y. Sun, J. Xu, L. Liang, H. Ju, J. Zhu, Y. Pan, W. Yan, Y. Lin and Y. Xie, *J. Am. Chem. Soc.*, 2017, **139**, 18044–18051.
- 31 J. Chen, Z. Wang, H. Lee, J. Mao, C. A. Grimes, C. Liu, M. Zhang, Z. Lu, Y. Chen and S. P. Feng, *Mater. Today Phys.*, 2020, **12**, 100176.
- 32 L. Yu, X. Ba, M. Qiu, Y. Li, L. Shuai, W. Zhang, Z. Ren and Y. Yu, *Nano Energy*, 2019, **60**, 576–582.
- 33 Z. Wang, J. Fan, B. Cheng, J. Yu and J. Xu, *Mater. Today Phys.*, 2020, **15**, 100279.
- 34 F. Zhang, Y.-H. Li, M.-Y. Qi, Z.-R. Tang and Y.-J. Xu, *Appl. Catal., B*, 2020, **268**, 118380.